

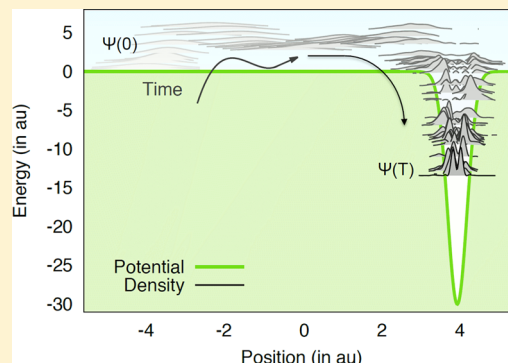
Steered Quantum Dynamics for Energy Minimization

Micheline Soley, Andreas Markmann, and Victor S. Batista*

Department of Chemistry, Yale University, P.O. Box 208107, New Haven, Connecticut 06520-8107, United States

Energy Sciences Institute, Yale University, P.O. Box 27394, West Haven, Connecticut 06516-7394, United States

ABSTRACT: We introduce a quantum optimal control algorithm for energy minimization that combines the diffeomorphic modulation under observable response preserving homotopy (D-MORPH) gradient and the Broyden Fletcher Goldfarb Shanno (BFGS) iterative scheme for nonlinear optimization. An extended set of controls defining the time-dependent mass, dipole moment, and external perturbational field are optimized to find an effective Hamiltonian that steers the dynamics of the system into the global minimum without getting trapped into local minima. The algorithm is illustrated as applied to energy minimization on rugged surfaces and golf potentials comparable to those previously explored for testing quantum annealing methodologies.



1. INTRODUCTION

The development of optimization methods for energy minimization continues to be a challenge at the forefront of computational scientific research. Over the years, many classical methods have been established and are routinely applied for studies of geometry optimization, protein folding, drug docking, and electronic structure calculations, including approaches based on classical mechanics with gradients,¹ molecular dynamics,^{2–4} direct search algorithms,^{5–7} and simulated annealing.^{8–10} One of the usual challenges faced by optimization on rugged potential energy surfaces, however, is trapping at local minima. Other challenges of classical methods include the search of narrow minima on flat potential energy surfaces, as in the so-called “golf problem”.¹¹ Nonclassical optimization methods offer several alternatives, including branch-and-bound methods,^{12,13} clustering techniques,^{14,15} tabu search,^{16,17} hybrid methods,¹⁸ and algorithms inspired by nature such as Evolutionary Algorithms (Genetic Algorithms,^{19,20} Evolutionary Programming,²¹ and Genetic Programming^{22,23}), the Ant System,²⁴ and Particle Swarm Optimization.²⁵ However, every optimization method has limitations in terms of accuracy or computational efficiency. Therefore, the development and implementation of novel algorithms remains a topic of great interest. This paper is focused on a quantum optimal control algorithm with an extended set of controls that allows for global optimization without trapping into local minima.

Potential smoothing techniques have been developed over the past 20 years to reduce the number of local traps and facilitate global optimization.^{11,26–29} Some of these methods include quantum annealing,^{11,26–30} packet annealing,³¹ Gaussian density annealing (GDA),³² the diffusion equation method (DEM),^{33,34} the ant-lion method,³⁵ and the potential shift method.³⁶ Several of these algorithms use quantum dynamics to take advantage of tunneling and the delocalized nature of the

quantum state probing the potential surface.^{37,38} Quantum annealing methods have been shown to be more effective than classical annealing for the Ising spin glass,³⁹ Lennard-Jones clusters,^{26,29} the traveling salesman problem,⁴⁰ the graph coloring problem,⁴¹ and protein folding,^{42,43} although significantly less successful than classical annealing for the more difficult random Boolean satisfiability problem.⁴⁴ Despite the advancements of potential smoothing methods, however, global optimization of the “golf problem” (i.e., a shallow parabola with a distant narrow hole) remains particularly challenging and a benchmark problem for directed optimization algorithms.^{11,42,45–51}

This paper introduces the Quantum Optimal Control Optimization (QuOCO) algorithm for numerically solving the general problem of finding the value of x that minimizes $V_0(x)$. As an example, we consider a particle with coordinates x on a potential energy surface $V_0(x)$. Building upon optimal control techniques,^{52–60} QuOCO couples the particle to an external field that steers it to the global minimum of $V_0(x)$. At the end of the propagation, the particle position serves as a pointer to the coordinates of the minimum. The minimization problem is thus reduced to the task of adjusting the parameters of the field (as well as the parameters that define the mass and dipole of the particle) to ensure that the system is found at the global minimum after a finite propagation time $T = t_f - t_0$. Therefore, instead of minimizing $V_0(x)$ with respect to x , QuOCO maps the optimization problem into a higher dimensional space: the space of control parameters that define the external field, mass, and dipole. The advantage of QuOCO,

Special Issue: William L. Jorgensen Festschrift

Received: May 12, 2014

Revised: July 28, 2014

Published: August 3, 2014

when compared to minimization of $V_0(x)$ with respect to x , is that the algorithm can avoid trapping at local minima of $V_0(x)$ by systematically increasing the dimensionality of the optimization problem (i.e., adding controls to the field, mass, and dipole).

Initially, QuOCO exploits quantum effects to explore classically forbidden regions on the potential energy surface. The resulting dynamics in turn provide feedback for optimization of the control parameters defining the perturbational field and the system time-dependent mass and dipole moment. Upon optimization of the controls, however, the system typically “flies” over all obstacles like a “quantum drone” and lands as a localized state at the global minimum after propagation for time T . Optimization of the controls with respect to $\langle \hat{V}(T) \rangle$ could in principle be based on traditional approaches. For computational efficiency, however, QuOCO implements the D-MORPH gradient in conjunction with the BFGS optimization method. An advantage of the D-MORPH gradient when compared to traditional methods is that it allows for evaluation of the gradients for all N control variables with only four propagations of the quantum state.⁶⁰ In contrast, traditional methods based on calculations of the control gradients by finite differences require at least $N + 1$ evaluations of $\langle \hat{V}(T) \rangle$, making the overall computational effort daunting when each evaluation requires propagation of the wave packet for time T . Another distinct aspect of QuOCO is the implementation of the D-MORPH gradient with BFGS optimization, which is much more efficient than integration of the controls by Runge–Kutta,⁶⁰ and the optimization of controls beyond those of the perturbational field, including parameters for the time-dependent dipole and effective mass. The extended set of controls allows for global optimization, without trapping into local minima, as illustrated in section 3 for several challenging potentials, including minimization on the golf potential previously explored for testing quantum annealing methodologies as well as more challenging potential energy surfaces with multiple minima.

2. METHOD

2.1. Optimization. To find the global minimum of a given function $V_0(x)$, QuOCO simulates the evolution of a particle of mass m on that potential energy surface $V_0(x)$ and under the influence of a perturbational field $E(t, \beta)$, as described by the time-dependent Hamiltonian:

$$\hat{H}(t; \beta) = \frac{\hat{p}^2}{2m(t, \beta)} + \hat{V}(x, t, \beta) \quad (1)$$

where $\hat{V}(x, t, \beta) = V_0(x) - \mu(x, t, \beta) \cdot E(t, \beta)$, with $\mu(x, t, \beta)$ the time-dependent dipole moment and $\beta = (\beta_1, \dots, \beta_N)$ the adjustable control parameters. The mass of the system $m(t, \beta)$ is also assumed to be time-dependent and determined by the controls. For simplicity, we consider notation in atomic units, so $\hbar = 1$, the electron mass $m_e = 1$ au, the electron charge $q_e = 1$ au, and the permittivity of a vacuum $4\pi\epsilon_0 = 1$ au.

The aim is to find parameters β so that the initial state $\psi_i = \psi(t_0)$ can evolve into a final state $\psi_f(\beta) = U(t_f, t_0; \beta)\psi(t_0)$, at time $T = t_f - t_0$, that minimizes the expectation value of the potential energy:

$$\begin{aligned} \langle \hat{V}_0(T; \beta) \rangle &= \langle \psi_f(\beta) | V_0(x) | \psi_f(\beta) \rangle, \\ &= \langle \psi_i | \hat{V}_0(T, x; \beta) | \psi_i \rangle \end{aligned} \quad (2)$$

Here, $\hat{V}_0(T, x; \beta) = U^\dagger(t_f, t_0; \beta)V_0(x)U(t_f, t_0; \beta)$ with the time-evolution operator,

$$U(t, t_0; \beta) = e^{-i/\hbar \int_{t_0}^t \hat{H}(t'; \beta) dt'} \quad (3)$$

To minimize $\langle \hat{V}_0(T; \beta) \rangle$, the parameters β can be optimized by following a path in control space, parametrized by a scalar s , as follows:

$$\beta_j(s + \Delta s) = \beta_j(s) + \frac{\partial \beta_j(s)}{\partial s} \Delta s \quad (4)$$

with gradients defined in terms of the gradients of $\hat{V}_0(T; \beta)$ with respect to the controls, as in the D-MORPH method:

$$\frac{\partial \beta_j(s)}{\partial s} = - \frac{\partial \langle \hat{V}_0(T; \beta) \rangle}{\partial \beta_j} \quad (5)$$

to ensure that $\langle \hat{V}_0(T, x; \beta) \rangle$ would decrease monotonically along that path, as follows:

$$\begin{aligned} &\langle \hat{V}_0(T, x; \beta(s + \Delta s)) \rangle \\ &\approx \langle \hat{V}_0(T; \beta(s)) \rangle + \sum_j \frac{\partial \langle \hat{V}_0(T, x; \beta) \rangle}{\partial \beta_j} \frac{\partial \beta_j(s)}{\partial s} \Delta s \\ &= \langle \hat{V}_0(T, x; \beta(s)) \rangle - \sum_j \left| \frac{\partial \langle \hat{V}_0(T; \beta) \rangle}{\partial \beta_j} \right|^2 \Delta s \end{aligned} \quad (6)$$

Equation 4, with gradients defined according to eq 5, can be integrated numerically by using the fourth-order variable step-size Runge–Kutta (RK) solver,^{61,62} obtaining the optimal controls. However, such a method is computationally demanding since the gradients need to be evaluated several times per integration step. Nevertheless, it provides detailed information on the control landscape and has been previously implemented to find controls that maintain an observable expectation value.⁶⁰ Here, the QuOCO algorithm implements it to find the set of controls that optimize the expectation value of the observable $\langle \hat{V}_0(T; \beta) \rangle$.

A more efficient approach is to use the Broyden–Fletcher–Goldfarb–Shanno (BFGS)^{63–69} and limited memory Broyden–Fletcher–Goldfarb–Shanno with boundaries (L-BFGS-B)^{70–72} optimization methods to minimize $\langle \hat{V}_0(T; \beta) \rangle$ with respect to the controls β without integrating eq 4. These methods perform far fewer evaluations of the landscape gradient (each requiring four propagations) and where possible use line minimizations (each requiring one propagation) instead. A comparison of performance of BFGS and L-BFGS-B versus fourth-order Runge–Kutta is presented in section 3.1.3, showing that BFGS, specifically L-BFGS-B, is the most effective optimizer for QuOCO.

Both Runge–Kutta solution of eq 4 and BFGS optimizations require computations of the gradients of $\langle \hat{V}_0(T; \beta) \rangle$ with respect to the controls β , which are obtained by using the D-MORPH gradients (Appendix 1):^{54–60}

$$\begin{aligned} \frac{\partial \langle \hat{V}_0(T; \beta) \rangle}{\partial \beta_j} &= -\frac{i}{\hbar} \int_0^T dt [\langle \psi_B(t) | H_{\beta_j}(\beta, t) | \psi_C(t) \rangle \\ &\quad - \langle \psi_C(t) | H_{\beta_j}(\beta, t) | \psi_B(t) \rangle] \\ &= \frac{2}{\hbar} \int_0^T dt \text{Im}[\langle \psi_B(t) | H_{\beta_j}(\beta, t) | \psi_C(t) \rangle] \end{aligned} \quad (7)$$

where $H_{\beta_j} = (\partial \hat{H})/(\partial \beta_j)$. Here, $|\psi_C(t)\rangle = U(t, 0; \beta)|\psi_i\rangle$ is obtained by forward propagation of the initial state $|\psi_i\rangle$. The state $|\psi_B(t)\rangle = U(t, 0; \beta)|\psi_A\rangle$ is obtained by forward propagation of the state $|\psi_A\rangle = U^\dagger(T, 0; \beta)V_0(x)U(T, 0; \beta)|\psi_i\rangle$ previously prepared by forward and backward propagation. Compared to a naïve finite-differencing approach, if the gradient of the Hamiltonian is known, the D-MORPH gradient is analytically exact as well as computationally more efficient. Instead of $N + 1$ propagations for finite differencing, four propagations are sufficient to evaluate the D-MORPH gradient: two propagations for time T for the calculation of ψ_A and two forward propagations for time T for the simultaneous forward propagation of ψ_B and ψ_C . Considering that QuOCO involves increasing the number N of control parameters β_j until a trap-free landscape is obtained, the constant scaling of the D-MORPH gradient is vital to the success of QuOCO.

2.2. Propagation. Wavepackets are propagated according to the split operator Fourier transform (SOFT) method.^{73–75} The time-evolving state $\psi(t)$ is expanded in the basis set of n equidistant delta functions $\delta(x - x_k)$, distributed in the range of coordinates $x_{\min} - x_{\max}$ with $x_k = x_{\min} + (x_{\max} - x_{\min})(k - 1)/(n - 1)$, where $k = 1 - n$. Propagation for a short time τ is accomplished by applying the time-evolution operator, as defined by the Trotter expansion:

$$e^{-i\hat{H}\tau} = e^{-i\hat{V}\tau/2}e^{-i\hat{p}^2/2m\tau}e^{-i\hat{V}\tau/2} + O(\tau^3) \quad (8)$$

as follows:

$$\psi(t + \tau) = e^{-i\hat{V}\tau/2} \int dp e^{ipx} e^{-i\hat{p}^2\tau/2m} \frac{1}{2\pi} \int dx' e^{-ipx'} e^{-i\hat{V}\tau/2} \psi(t) \quad (9)$$

where $\hat{V} \approx \hat{V}(x, t, \beta)$ and $m \approx m(t, \beta)$ during the propagation time increment τ .

In this study we focus on one-dimensional model systems. However, applications to higher dimensional problems could be performed analogously by using other wavepacket propagation schemes such as the MP/SOFT method.^{76–83} Other methodologies for quantum propagation on higher dimensional potentials include Coupled Coherent States (CCS)^{84,85} and Multi-Configurational Ehrenfest (MCE) dynamics,^{86–88} the Multiple Spawning (MS) methods Full Multiple Spawning (FMS)^{89,90} and ab initio Multiple Spawning (AIMS),^{91,92} the Herman-Kluk semiclassical (HKSC) approximation,^{93,94} the time-dependent Gauss-Hermite (TDGH) method,^{95–97} and the Gaussian Multiconfigurational Time-Dependent Hartree (G-MCTDH)^{98,99} and variational Multiconfigurational Gaussians (vMCG) methods.^{100,101}

2.3. Control Parameters. **2.3.1. Perturbational Field.** Control parameters c_i and s_i determine the perturbational field, as follows:

$$E(t) = \sum_{i=1}^{N_c/2} s_i \sin(\omega_i t) + c_i \cos(\omega_i t) \quad (10)$$

According to eq 10, the partial derivatives of the Hamiltonian with respect to c_i and s_i are

$$H_{s_i} = -\mu(x, t) \sin(\omega_i t) \quad (11)$$

$$H_{c_i} = -\mu(x, t) \cos(\omega_i t) \quad (12)$$

We note that the expression of $E(t)$, introduced by eq 10, is not necessarily representative of a realistic perturbational field with

a finite temporal profile. In our initial attempts, a physically realistic field envelope with a \sin^2 shape for the temporal profile was employed with much less success than when using eq 10.

The results reported in section 3 were obtained by optimization of the controls after initializing the field coefficients as $s_i = 0.003$ and $c_i = 0.008$. These values were deliberately chosen to demonstrate the capabilities of the optimization procedure by ensuring that the initial perturbational field would not induce localization of the wave function in the global minimum. The lowest six frequencies from the reciprocal space of the corresponding temporal grid,

$$\omega_j = \frac{2\pi}{T} \cdot j, \quad j = 0, \dots, N_c/2 \quad (13)$$

were used for eq 10, unless otherwise indicated. The number of frequencies was chosen to balance the computational effort and freedom in control space, as discussed in section 3.1.2.

2.3.2. Dipole Moment. Control parameters γ_{sjn} and γ_{cjn} define the time-dependent dipole moment, as follows:

$$\mu(x, t) = \sum_{j,n} \left[\gamma_{sjn} \sin\left(k_j x + l_n \frac{2\pi}{T} t\right) + \gamma_{cjn} \cos\left(k_j x + l_n \frac{2\pi}{T} t\right) \right] \quad (14)$$

for a given set of constants k_j and l_n . The partial derivatives of the Hamiltonian with respect to these control parameters are

$$H_{\gamma_{sjn}} = -E(t) \sin\left(k_j x + l_n \frac{2\pi}{T} t\right) \quad (15)$$

$$H_{\gamma_{cjn}} = -E(t) \cos\left(k_j x + l_n \frac{2\pi}{T} t\right) \quad (16)$$

The optimized shape of the dipole moment is critical since it determines the probe-field interaction according to the following force:

$$F(x) = -\nabla V(x) \quad (17)$$

$$F(x, t) = -\nabla V_0(x) + \nabla \mu(x, t) \cdot E(t) \quad (18)$$

The nonuniform force, given by eq 18, ensures a finite gradient throughout space that is critical for inducing localization of the wavepacket at the global minimum in spite of the intrinsic delocalization induced by propagation.

Initially, various functional forms for time-independent dipole moments were tested, including e^x , $\arctan(x)$, $\text{erf}(x)$, $\tan(x)$, and $e^x \sin((\pi(x - x_{\min}))/((x_{\max} - x_{\min})))$, although with only moderate success. From these forms, e^x was the most advantageous, although not always successful due to numerical problems and the limited success of exponential dipoles in mediating the coupling with the field $E(t)$. The main limitation was that they provided a single set of gradients at each position. Results, reported in Sec. 3, were obtained by initializing the dipole controls to unity (i.e., $\gamma_{sj} = \gamma_{cj} = 1.0$). Such initialization ensured that the system did not localize at the global minimum during the initial propagation for time T and that, only after optimization of the controls, localization at the minimum was achieved despite the deliberately chosen adverse starting conditions.

2.3.3. Mass. The complete set of controls also includes parameters ϑ_p defining the time-dependent mass, as follows:

$$m(t) = \sum_{j=0}^{T/\tau} \vartheta_j \delta(t - t_j) \quad (19)$$

where $t_j = j\tau$, with τ the propagation time increment, introduced in section 2.2. The window functions δ are defined as $\delta(t - t_j) = 1$ for $|t - t_j| < \tau/2$ and $\delta(t - t_j) = 0$ otherwise. From eq 19, we obtain the derivative of the Hamiltonian with respect to the controls ϑ_j , as follows:

$$H_{\vartheta_j} = -\frac{p^2}{2m^2} \delta(t - j\tau) \quad (20)$$

In initial attempts, a particle with a constant mass was used. Due to only partial success, a time-dependent mass of the form

$$m(t) = m_0 + (m_f - m_0) \left(\frac{t}{T} \right)^P \quad (21)$$

was subsequently introduced, where m_0 and m_f were the initial and final values of the mass, and P was the power of the mass change rate. The motivation was to start with a low value for the mass that would facilitate ballistic motion and then increase the value to facilitate localization at the global minimum. However, best performance was achieved when the mass value was optimized at each time during the propagation. This was accomplished by using the summation of delta functions, given by eq 19, and the L-BFGS-B constrained BFGS optimization algorithm to ensure that the mass had physically realistic values during the optimization.

2.4. Temporal Grid. The total propagation time $T = t_f - t_0$ and the integration time step increment τ must be tuned according to the problem of interest to ensure convergence of the results with respect to both of these parameters. Increasing T allows the wave function to probe a more extended region of the potential energy surface and gives more time to the perturbational field to steer the evolution of the wavepacket into the global minimum. Concurrently, an increase in the total number of time steps incurs greater computational cost. Therefore, the temporal grid parameters must be chosen to balance the benefits of flexibility and control, as mentioned below, with the greater cost of an increased number of time steps. Section 3 shows that a very modest number of propagation time steps (14–50) is often sufficient for successful optimization.

The temporal grid determines the range of perturbational field frequencies available for optimization. The frequencies that define the perturbational field according to eq 10 should be represented on the corresponding reciprocal temporal grid. Each frequency must be in the range $(2\pi)/T < \omega \leq \pi/\tau$, where adjacent frequencies are separated by $(2\pi)/T$. Thus, increasing T decreases the minimum value of the frequency and increases the total number of possible frequencies. Decreasing the time step τ increases the maximum value of the frequency.

A greater frequency range gives more flexibility to the field to steer the wave function from its initial position to the global minimum. As two perturbational field controls are used for each frequency (s_i and c_i) in eq 10, a greater number of frequencies also allows for more field controls. A greater number of field controls in turn allows for more freedom in control space to aid global optimization. Moreover, changes in the temporal grid affect the dipole temporal constants l_n in eq 14 as well as the perturbational field frequencies.

The number of mass controls introduced by eq 19 is also determined by the temporal grid. Increasing the number of

time steps by increasing the propagation time T or decreasing the time step τ increases the total number of mass controls and allows the mass to change more often over the propagation time, as each time step has one control ϑ_j . In addition, a smaller time step τ reduces the minimum possible mass by reducing the minimum momentum that can be represented on the corresponding temporal grid.

2.5. Position Grid. When implementing the quantum propagation, as described in section 2.2, with the time-dependent wave function represented on a grid of n equidistant delta functions $\delta(x - x_k)$ with $x_k = x_{\min} + (x_{\max} - x_{\min})(k - 1)/(n - 1)$, where $k = 1 - n$, it is important to include an extended range of coordinates ($x = x_{\min} - x_{\max}$) consistent with the initial conditions and the total propagation time T . The position grid must also provide a sufficient number of dipole control parameters. In the same way that the choice of the temporal grid (discussed in section 2.4) determines the available perturbational field frequencies in eq 10 and dipole temporal constants l_n in eq 14, the position grid determines the available dipole position constants k_j in eq 14. The dipole position constants must be represented on the position grid, such that each dipole position constant is in the range $(2\pi)/(x_{\max} - x_{\min}) < k_j \leq \pi/(\Delta x)$ with adjacent constants separated by $(2\pi)/(x_{\max} - x_{\min})$. The position range gives the lowest available constant and the separation between adjacent constants, while the distance between neighboring position grid points gives the highest available constant. This is critical for optimization of the dipole and ultimately successful optimization.

The results discussed in section 3 are based on grids with $n = 2^{10}$ grid points in the $x = [-10, 10]$ au range. The initial state of the system was chosen as a Gaussian

$$\psi_i(x) = \sqrt{\frac{\alpha}{\pi}} \exp\left(-\frac{\alpha}{2}(x - x_k)^2 + ip_k(x - x_k)\right) \quad (22)$$

where $\alpha = 1$ is a constant, x is the position, x_k is the initial position, and $p_k = 0$ au is the initial momentum. In the study, x_k was varied to demonstrate the ability of QuOCO to locate the global minimum in high-energy and low-energy cases despite unhelpful positioning of the initial state. In general purpose applications, the initial state could be chosen according to what is known about the surface to be analyzed and simulations based on various different initial conditions could be compared.

3. RESULTS AND DISCUSSION

The presentation of results is organized as follows. Section 3.1 illustrates the QuOCO methodology as applied to asymmetric double wells with various levels of complexity as determined by the size of the barrier, the asymmetry of the wells, and the initial conditions, and includes an extended discussion of the optimization procedure and the parameters involved. Then, section 3.2 demonstrates the algorithm as applied to more challenging benchmark model potentials, including multiwell potentials and the golf problem.

3.1. Benchmark Double Well Potentials. We have implemented the DMORPH gradient and applied it with an RK solver and BFGS optimizers to the search of global minima in benchmark potential energy surfaces, defined as follows:

$$V(x) = \frac{1}{2}m_0\omega^2(x - x_1)^2 - D \exp\left(-\frac{(x - x_g)^2}{2\sigma^2}\right) \quad (23)$$

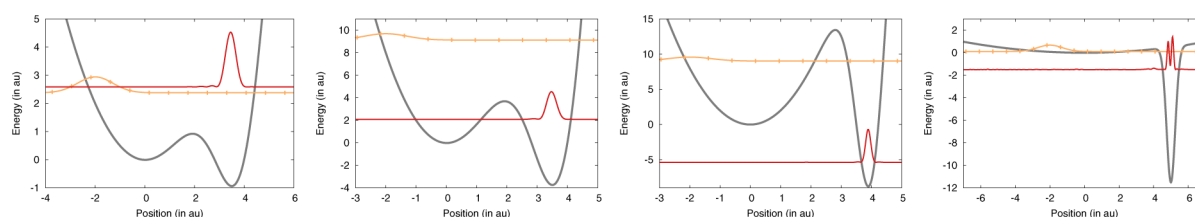


Figure 1. Final states localized at the global minima (red lines) obtained by QuOCO steered quantum dynamics of the initial states (orange lines) on asymmetric double-wells (gray lines) parametrized according to Table 1 (from left to right: surfaces 1–4). The initial states (orange lines) are defined according to eq 22, with $x_k = -2.0$, $p_k = 0$, and $\alpha = 1$. Base lines of quantum densities indicate total energy.

Figure 1 and Table 1 show that the QuOCO methodology is successful for both the RK solver and the BFGS optimizer but

Table 1. Parameters (in au) for Model Hamiltonians of Benchmark Systems with Double-Well Potential Energy Surfaces, Defined by Eq 23, with Mass $m(t)$ Defined by Eq 21, where $m_0 = 1$ au and $P = 2^a$

| surface | ω | σ | D | T | m_f | BFGS | RK |
|---------|----------|----------|-----|----------|--------|------|------|
| 1 | 1 | 1 | 8 | 16τ | $2m_0$ | 591 | 7347 |
| 2 | 2 | 1 | 32 | 14τ | $2m_0$ | 240 | 4396 |
| 3 | 2 | 0.5 | 40 | 19τ | $4m_0$ | 752 | 9821 |
| 4 | 0.2 | 0.25 | 12 | 47τ | $4m_0$ | 397 | 1958 |

^aThe number of propagation runs required for optimization of the controls by using BFGS optimization and RK solver methods are reported in the columns marked BFGS and RK, respectively.

that BFGS delivers superior efficiency, employing between 80 and 95% fewer propagation runs.

The complexity of the surface is modulated by changing the various parameters, including ω that defines the curvature (i.e., shallowness of the surface), D is the depth of the global minimum, σ is the width of the global minimum basin, and x_l and x_g are the positions of local and global minima, respectively. Note that m_0 is the particle mass at the initial time only, so interpreting ω as frequency is incorrect at later times, when the mass is adapted.

The analysis of convergence, relative to the total propagation time T , shows that a very modest number (14–47) of time steps are necessary for global minimization on these potential energy surfaces. Benchmark calculations for surfaces 1–3 required a final propagation time shorter than $T = 20\tau$ (with

$\tau = 0.2$ au). Localization of the final wave function in a narrow minimum, as in surface 4, typically requires longer propagation times (e.g., 50τ) because of the lower number of bound states and greater zero point energy.

3.1.1. Steered Quantum Dynamics. The optimized controls determined by QuOCO minimization of $\langle \hat{V}(T) \rangle$ define the time-dependent perturbational field, dipole, and mass to be used to obtain a final state with minimum potential energy at time T . The expectation value of the position $\langle \hat{x}(T) \rangle$ then pinpoints the location of the global minimum on the surface. Therefore, the resulting optimization determines the coordinates of the global minimum and the values of the controls necessary to steer the dynamics of the system to the global minimum of the potential energy surface.

Figure 2 shows the final states (red lines) obtained for potential energy surfaces (1) and (4) of the form given by eq 23 and intermediate results obtained during optimization of the controls after 0 (solid blue), 30 (dashed blue), 45 (dotted blue), and 72 (solid red) optimization iterations (left panel).

These results show how successive iterations lead to a state that pinpoints the global minimum. The initial state position was defined for $x_k = 0.0$ au and the propagation time was $T = 50\tau$, with $\tau = 0.1$ au. Here, we used 50 mass controls with initial guess values $m(t) = 1$ au + $(7 \text{ au})/(t/T)^2$, 12 field controls for the lowest six frequencies on the reciprocal temporal grid, and 10 dipole controls with initial guess values $\gamma_{xj} = 1.0$ for dipole constants consisting of all possible combinations of $k_j = (2\pi j)/(x_{\max} - x_{\min})$, $l_n = (\pi n)/(\Delta x)$, where $j = 0, \dots, 5$, $l = 0, \dots, (N_\gamma)/(10) - 1$ in a dipole of the form of eq 14. For L-BFGS-B optimization, $M = 5$ correction pairs, a function tolerance $F_{\text{tol}} = 10^{12}$ (where $(F_k - F_{k+1})/(\max\{|F_k|, |F_{k+1}|\}) \leq F_{\text{tol}} \cdot \epsilon_{\text{machine}}$), with

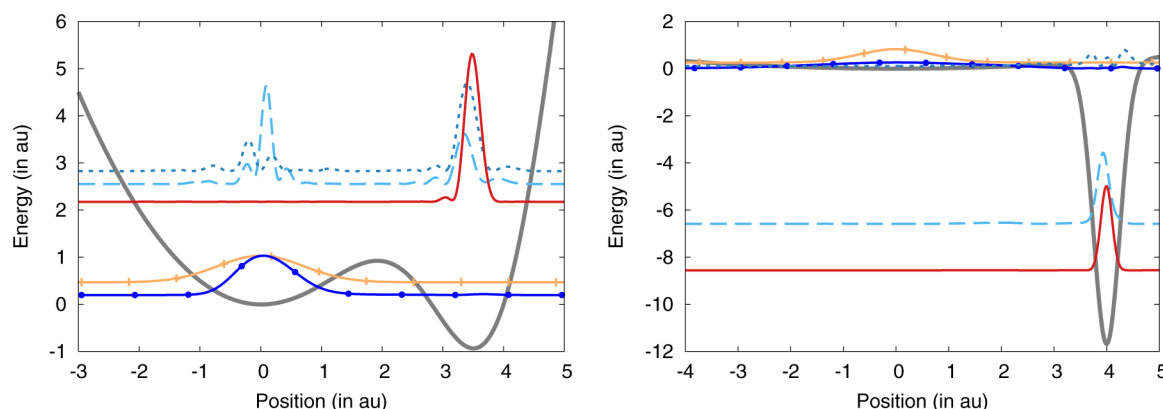


Figure 2. Left: Final state obtained through iterative optimization of the controls by wavepacket propagation of an initial guess (dotted orange) after 0 (solid blue), 30 (dashed blue), 45 (dotted blue), and 72 (solid red) iterations, showing how the initial state (dotted orange) is driven by the external field into an optimized final state (solid red) localized at the global minimum of the potential energy surface (solid gray). Right: Analogous results for a shallow surface with a distant narrow minimum after 0, 6, 31, and 59 iterations. Base lines of quantum densities indicate total energy.

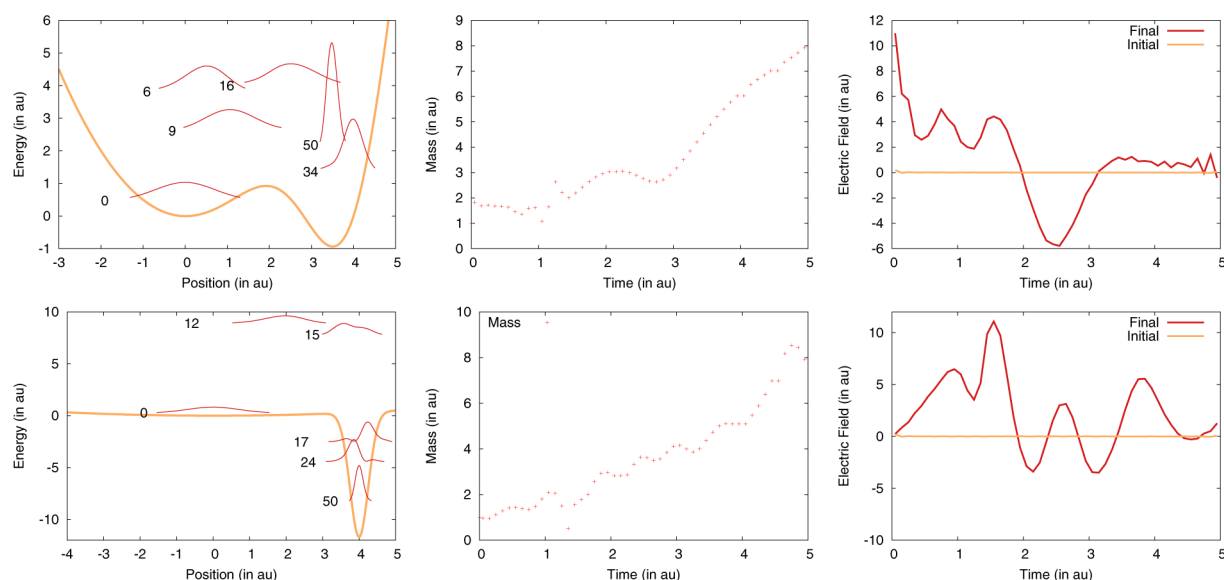


Figure 3. Evolution of wave packets (red lines) in the potential surface (orange line) based on steered quantum dynamics with fully optimized controls, as they propagate from the initial state (0 time steps) to the final state (after 50 time steps). Fully optimized mass and perturbational field time-dependence are shown in the center and right panels, respectively.

F_k the function value for the k th iteration and $\epsilon_{\text{machine}}$ the machine precision), and a projected gradient tolerance $G_{\text{tol}} = 10^{-5}$ (where $G_{\text{tol}} = \max\{|G_i|_{i=1,\dots,N}\}$ and G_i is the projected gradient in the direction of control i) were used to balance the accuracy of high M and F_{tol} and low G_{tol} values with the computational efficiency of low M and F_{tol} and high G_{tol} .

Figure 3 (left) shows how the initial states (red) are driven from the initial state (0 time steps) to the final state (after 50 time steps) according to steered quantum dynamics based on optimized controls.

In addition, Figure 3 shows the optimized time-dependent mass and perturbational field (center and right panels, respectively). Initially, the system has low mass and is therefore influenced by the perturbational field. In both examples, the system gains energy from the field (time steps 1–16) until it is well over the energy barrier separating the local and global minima. Then, it is pulled toward the global minimum. The strength of the perturbational field diminishes as the wave function reaches the global minimum well. Simultaneously, the mass increases to aid localization of the particle in the global minimum (time step 50).

3.1.2. Control Space Dimensionality. Theoretically, for a sufficiently large number of controls β_j , the minimization becomes free of suboptimal traps.^{54–56} The premise of such a theorem is that the Hamiltonian can be written as a matrix made up of elements that can be individually varied by the controls β . In an infinite-dimensional space, this assumption can be reached only asymptotically. Nevertheless, we can add control variables systematically through a delta function expansion of the mass dependence and the Fourier expansions of the field and dipole. We can also add time steps by either increasing the total time or decreasing the time step. In fact, we can asymptotically approach a scenario in which vectors in control space individually vary each of the Hamiltonian's elements in the matrix representation of the eigenstates populated during the propagation. For our processes, it is evident that the target can be reached via a finite energy path involving only finitely many low-energy eigenstates of the system, so that a finite Hamiltonian matrix results that can be

fully controlled with finitely many control variables β_j . Since we have a systematic way of adding control variables, we can reach any number of controls that may be required to take advantage of this aspect of the D-MORPH gradient.

The QuOCO methodology should always find the global minimum, given enough controls and sufficiently long propagation time T . As discussed in section 2.1, increasing the number of controls does not increase the number of wavepacket propagations, although the computational effort may increase with the number of controls since more optimization iterations may be needed for the search in a higher-dimensional space. Therefore, it is important to tune the number of controls to optimize the underlying computational cost while keeping the dimensionality of the control space sufficiently large. In practice, the current implementation requires a sufficient number N_c of perturbational field controls and N_γ dipole controls to allow the dipole-field interaction to direct the initial wave function into the global minimum. The number of mass controls N_θ must allow the mass to begin low enough for the particle to be moved to the global minimum well and sample a large enough area of the potential surface through quantum dispersion and tunneling. It must also be able to become high enough for the system to sufficiently localize in the global minimum well at the end of the propagation.

The number of controls of each type can be chosen to balance the ability of the optimizer to maneuver in control space with high computational efficiency. To explore this balance, the computational time necessary to locate the global minimum of surface 1 was compared for various combinations of controls. Increasing N_γ and N_θ was shown to increase the computational run time linearly with the number of controls. As each mass control θ_j is associated with a single time step in the propagation via eq 19, increasing the number of mass controls N_θ linearly increases computational effort. However, the impact of N_γ and N_c is dominated by their impact on the size of the search space for the optimizer.

In contrast, a subconstant scaling with respect to N_c was observed. This is likely due to the fact that more control parameters may open up shortcuts in control space for trap-free

global minimization, as discussed in section 2.1.^{54–56} In fact, we find that increasing the number of field controls N_c , given a suitable number of dipole controls N_d and mass controls N_g , serves to decrease linearly the computational time necessary for location of global minima, providing an efficient path to the global minimum.

3.1.3. Potential Energy Optimization. The D-MORPH gradient offers significant advantages over finite differencing methods for calculations of the gradients of the expectation value $\langle \hat{O}(T) \rangle$ with respect to the controls. While only four propagations are required according to eq 7, regardless of the number N of controls β_j , analogous calculations based on second order differencing require $N + 1$ propagations. Updating the controls according to eq 4 via solution of eq 5, however, is usually computationally demanding and requires intensive integration methods, such as fourth-order Runge–Kutta (RK) integration.⁶⁰ Here, we show that BFGS and L-BFGS-B nonlinear optimizers allow for significant gains in computational efficiency, typically converging 1 or 2 orders of magnitude faster than RK integration (Table 1 and Figure 4).

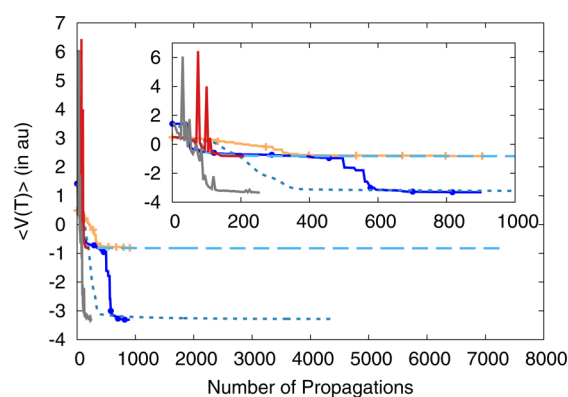


Figure 4. Expectation value of the potential energy $\langle \hat{V}(T) \rangle$ for two representative examples (labeled as surfaces 1 and 2, propagation time $T = 16\tau$) as a function of the number of propagation runs employed during optimization. Color key: L-BFGS-B optimizer (solid lines), red (surface 1) and gray (surface 2); RK solver (dashed lines), light blue (1) and dark blue (2); BFGS optimizer (dotted lines), orange (1) and blue (2). Magnification of the first 1000 steps in inset. The L-BFGS-B optimizer iterates not strictly monotonically but converges to the optimized result much more rapidly than the BFGS optimizer and RK solver.

Figure 4 shows the expectation value of the potential energy $\langle \hat{V}(T) \rangle$ for two representative examples (labeled as surfaces 1 and 2, for propagation time $T = 16\tau$, Figure 4) to illustrate the

relative performance of D-MORPH/RK and D-MORPH/BFGS. Both methods evolve the controls to an optimized set that localizes the wave function at the global minimum. However, D-MORPH/BFGS (specifically, D-MORPH/L-BFGS-B) minimization is significantly more efficient, requiring only 3–6% of the computational effort required by D-MORPH/RK with comparable tolerance.

Note that $\langle \hat{V}(T) \rangle$ decreases sharply to the global minimum for surfaces 1 and 2 after 150 and 125 propagations for L-BFGS-B optimization, after 100 and 380 propagations for RK solution, and after 430 and 760 propagations for BFGS optimization, respectively. The L-BFGS-B optimization tolerances were as detailed in section 3.1.1. A variable step size for the Runge–Kutta solution of eq 5 was used with a minimum step size of $\varepsilon_h = 10^{-12}$ au and abort condition with $\varepsilon_n = 10^{-6}$ au as the norm of the gradient. The abort condition was satisfied when the observable difference between consecutive iterations dropped below a set abort tolerance. Here, the observable is the potential expectation value at the final time of each propagation under controls β given by the iteration in control space. The abort tolerance is set so that the RK solver finds the global minimum and the BFGS optimizer performance is compared at the same tolerance.

An initial Runge–Kutta step size $\Delta s = 1$ au was used to maximize the length of each Runge–Kutta step. The BFGS optimization tolerances were manipulated to reproduce the results of QuOCO with Runge–Kutta. Fletcher values $\varepsilon_F = 10^{-4}$ for potential (3) and $\varepsilon_F = 10^{-3}$ for other surfaces were the maximum possible values that reproduced the expectation value of the potential energy $\langle \hat{V}(T) \rangle$ results from the Runge–Kutta solution of eq 5 for the potentials under study. The functional tolerance $\varepsilon_m = 10^{-4}$ accounted for the numerical error and was decreased to the minimum at which BFGS minimization was successful.

At comparable tolerances, both the RK solver and BFGS optimization methods resulted in a wave function localized in the global minimum after several hundred propagations of the wavepacket, at which point the rate of reduction of $\langle \hat{V}(T) \rangle$ decreased significantly but did not completely plateau. For example, for surface 2 with BFGS optimization, the global minimum well was clearly located by 251 propagations, even though 914 propagations were necessary for complete minimization. The minimization can be even more efficient if a BFGS optimization method is applied only until reaching the global minimum basin and then minimization is completed in a few optimizer iterations by a gradient-driven optimization.

3.1.4. Comparison to Potential Smoothing and Quantum Annealing. The energy contribution from the dipolar

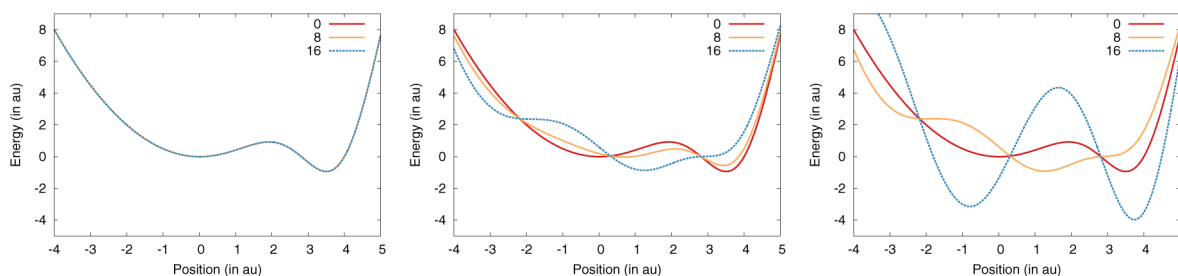


Figure 5. Effective potential $V(x) - \mu(x,t)E(t)$ steering dynamics toward minimum, at $t = 0$ (red), 8 (orange), and 16 τ (blue), with $\tau = 0.2$ au, for surface 1 (eq 23, Table 1), and perturbational field parametrized as $E = 0$ (left), with coefficients $s_i = c_i = 0.68$ (center), and optimal controls (right) as obtained by QuOCO.

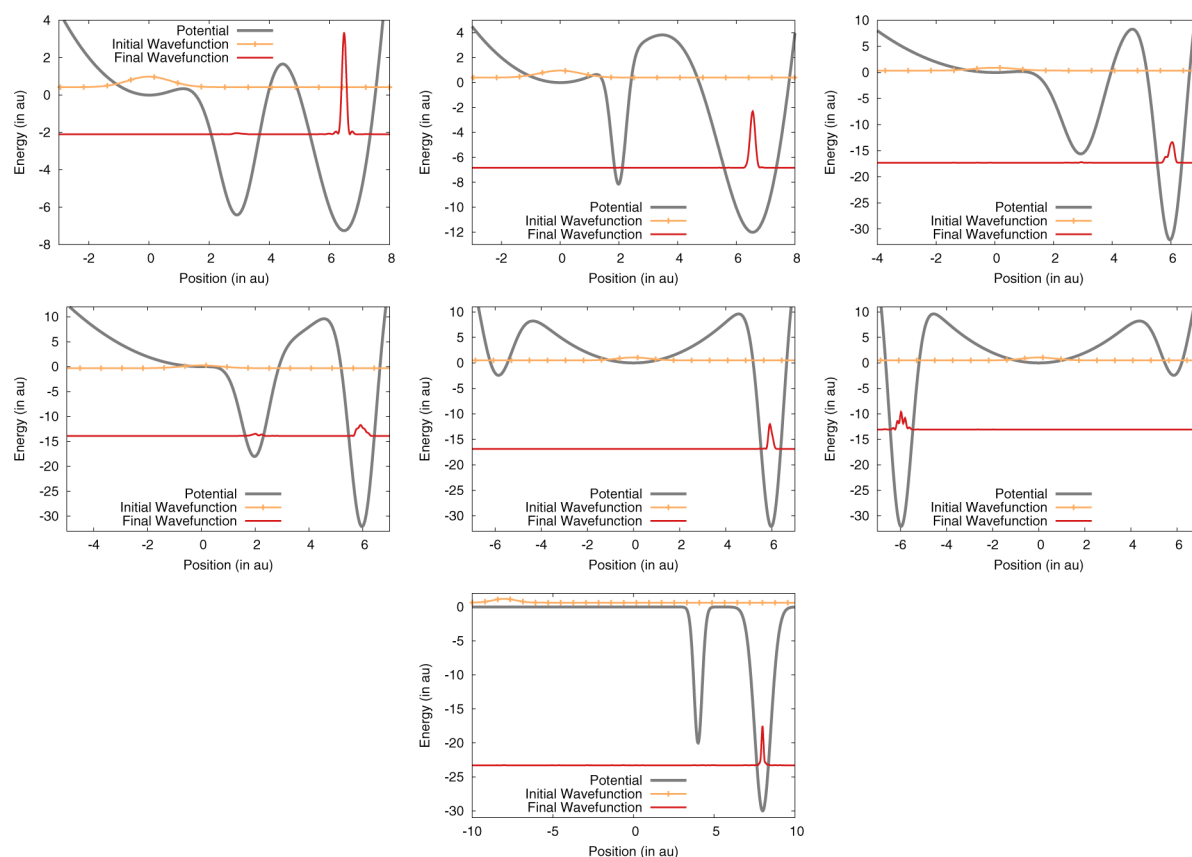


Figure 6. Final states (red line) after propagation of the initial state (orange line) with optimized controls found by QuOCO for six different triple-well potentials (gray line) from left to right (A)–(C), top row; (D)–(F), center row; and golf potential (G), bottom row.

interaction $-\mu(x,t)E(t)$ could overtly serve to remove the potential barrier separating the local and global minima as in potential smoothing methodologies. Therefore, it is important to analyze the net potential $V(x) - \mu(x,t)E(t)$ after optimization of the control parameters by QuOCO and assess whether optimization is in fact achieved by potential smoothing or steered quantum dynamics (Figure 5).

Figure 5 (center panel) shows that the dipolar interaction with fixed controls $s_i = c_i = 0.68$ reduces the barrier between the local and global minima, illustrating how an applied field may be used for potential smoothing. However, Figure 5 (right panel) shows that QuOCO optimization does not evolve the controls to smooth the effective potential but rather adapts the shape of the effective potential to steer the dynamics into the global minimum. While the effective potential might become barrierless during the propagation, at subsequent stages the barriers are re-established and serve to localize the system at the global minimum. Note, for example, that at the time 8τ , the original barrier has disappeared while a global minimum appears near the position of the original barrier. At time 16τ , however, a larger barrier appears at the location of the original barrier. In contrast, the effective potentials typically used by smoothing techniques are barrierless and remain static during the optimization.^{33,102,103}

The QuOCO method can also be compared to quantum annealing, which involves potential smoothing in conjunction with quantum propagation.^{26,27} A variable value of \hbar is typically decreased toward convergence to reduce the zero-point energy of the system at the minimum. In contrast, QuOCO keeps \hbar constant and localizes the state by increasing the mass. The

increased mass serves to decrease the zero-point energy. While physically distinct, the QuOCO Hamiltonian with variable mass can also be interpreted as a Hamiltonian with time-dependent \hbar and constant mass, so QuOCO could be thought of as a generalized version of quantum annealing that includes D-MORPH/BFGS optimization of the time-dependent \hbar as well as optimization of the time-dependent dipolar interaction with the perturbational field.

QuOCO and quantum annealing have common features as well as significant differences. Both methods are based on quantum propagation, exploit quantum effects (e.g., tunneling and interference) for exploration of the potential energy surface, and localize the state at the minimum by decreasing the zero-point energy. Whereas quantum annealing methods require stochastic sampling and repeated trials, QuOCO makes use of steered dynamics to reach the global minimum. In addition, QuOCO optimizes the parameters that define the mass, dipole, and perturbational field by using nonlinear D-MORPH/BFGS optimization and finds the controls that guide the initial state to the global minimum. Another difference is given by the requirements of the initial state. For quantum annealing to succeed, the initial state has to have some significant amplitude at the global minimum.²⁶ In contrast, QuOCO can be successful even if the initial state does not fulfill the requirements of quantum annealing, so long as the propagated state has some finite amplitude at the global minimum. Due to these features, QuOCO compares quite well in terms of performance, as shown in section 3.2, even for potentials more challenging than the most difficult golf potentials solved by potential smoothing techniques.¹¹

3.2. Multiple-Well and Golf Potentials. **3.2.1. Multiple-Well Potentials.** Figure 6 shows the capabilities of the QuOCO algorithm as applied to the search for global minima in benchmark potential energy surfaces with multiple wells of the form:

$$V = \frac{k}{2}x^2 - D \exp\left(-\frac{(x-x_0)^2}{2\sigma^2}\right) - D' \exp\left(-\frac{(x-x'_0)^2}{2\sigma'^2}\right) \quad (24)$$

where D , σ , and x_0 define the depth, width, and position of a deep well, respectively, while D' , σ' , and x'_0 define the corresponding parameters for another narrow well, according to the various sets of parameters listed in Table 2. The initial

Table 2. Parameters (in au) of Triple-Well Potentials and Golf Potential Defined by Eq 24

| case | ω | x_0 | D | σ | x'_0 | D' | σ' |
|------|----------|-------|-----|----------|--------|------|-----------|
| (A) | 1.0 | 3.0 | 10 | 0.7 | 7.0 | 30 | 1.5 |
| (B) | 1.0 | 2.0 | 10 | 0.25 | 7.0 | 35 | 1.5 |
| (C) | 1.0 | 3.0 | 20 | 0.7 | 6.0 | 50 | 0.5 |
| (D) | 1.0 | 2.0 | 20 | 0.5 | 6.0 | 50 | 0.5 |
| (E) | 1.0 | -6.0 | 20 | 0.7 | 6.0 | 50 | 0.5 |
| (F) | 1.0 | 6.0 | 20 | 0.7 | -6.0 | 50 | 0.5 |
| (G) | 0.0 | 4.0 | 20 | 0.25 | 8.0 | 30 | 0.5 |

guess values for the time-dependent mass were defined as $m_0(t) = 1 \text{ au} + (7 \text{ au})(t/T)^2$, and the propagation time $T = 80\tau$ with $\tau = 0.1 \text{ au}$. The initial state was defined according to eq 22, with $x_k = 0.0 \text{ au}$ for (A)–(F) and $x_k = -8.0 \text{ au}$ for (G). The initial guess dipole coefficients were defined as $\gamma_{xj} = 1.0$ and the dipole constants included all possible combinations of $k_j = (2\pi j)/(x_{\max} - x_{\min})$, $l_j = j$ for $j = 1, \dots, (N_\gamma)/2$ in a dipole of the form given by eq 14. The 30 lowest possible frequencies on the reciprocal temporal grid were used for perturbational field controls for all potentials except (D) and (G), for which all 40 possible frequencies were used. The numbers of dipole controls N_γ are listed in Table 3.

Table 3. Number of Dipole Controls N_γ , Expectation Value of the Potential Energy $\langle \hat{V}(T) \rangle$, Position $\langle \hat{x}(T) \rangle$, Position Standard Deviation (SD), and Number of Propagation Runs (# runs) for Model Potentials (A)–(G), shown in Figure 6

| case | N_γ | $\langle \hat{V}(T) \rangle$ | $\langle \hat{x}(T) \rangle$ | SD | # runs |
|------|------------|------------------------------|------------------------------|------|--------|
| (A) | 12 | -7.1 | 6.4 | 0.45 | 215 |
| (B) | 12 | -12 | 6.4 | 0.85 | 235 |
| (C) | 14 | -29 | 5.7 | 2.4 | 530 |
| (D) | 16 | -25 | 4.9 | 5.0 | 400 |
| (E) | 6 | -31 | 5.8 | 0.82 | 545 |
| (F) | 8 | -28 | -5.8 | 1.2 | 585 |
| (G) | 10 | -29 | 7.8 | 1.9 | 460 |

Figure 6 shows the final states (red line) obtained by propagation of the initial state (orange line), with optimized controls obtained by QuOCO. These results show that the algorithm is able to find the global minima for all six triple-well potentials (A)–(F) and the golf potential (G). Case (A), shown in the top-left panel of Figure 6, involves a state initially localized in a shallow local minimum next to a deep well separated from the global minimum by a large barrier. As shown by the position of the localized final state, QuOCO successfully finds the global minimum in several hundred

iterations. Case (B), shown in the top-center panel of Figure 6, is more challenging since it involves an initial state that is separated from a wide global minimum by a barrier that is both high and wide. Case (C) is even more demanding since it involves a narrower global minimum separated by a large barrier. Case (D) is even more difficult and requires a larger number of field controls, including all frequencies on the reciprocal temporal grid, since it involves a narrow global minimum separated by a higher barrier. Cases (E) and (F) show successful performance even for bifurcated dynamics of a state initially located in a shallow valley, showing that the optimization procedure is successful irrespective of the location of the global minimum well relative to the initial state. Finally, case (G) shows successful global minimization even when the potential is not bounded by a parabolic component.

In summary, benchmark calculations for the model systems shown in Figure 6 show that QuOCO exhibits successful performance despite the intrinsic challenges of high barriers, distant global minima, narrow wells, shallow initial valleys, fine separation between local and global minima, and bifurcation. Overall, QuOCO is a successful global minimization technique that avoids trapping into local minima, given a sufficient number of controls and sufficient propagation time.

3.2.2. Golf Potentials. For direct comparison with potential smoothing algorithms, QuOCO was evaluated as applied to “golf potentials” of the general form:¹¹

$$V(x) = x^2 - \sum_{i=1}^3 D_i \exp(-S_i(x - x_{0,i})^2) \quad (25)$$

where D_i , S_i , and $x_{0,i}$ are the depth, width, and position, respectively, for the i th well of the potential energy surface in a harmonic valley. Figure 7 shows the results of optimizations for four different golf potentials, parametrized as described in Table 4. The results of the optimizations are summarized in Table 5.

Figure 7 (left panel) shows that QuOCO is able to locate the global minimum of the golf potential (i), previously used as a benchmark model for testing quantum annealing methods.¹¹ In addition, Figure 7 shows the capabilities of QuOCO to solve even more difficult potentials of the same form, including potentials (ii)–(iv). Successful optimization required $N_c = 100$, $N_\gamma = 400$, and $N_\theta = 100$. The initial guess for the time-dependent mass was $m(t) = (99 \text{ au})(t/T)^2$ for model (i), $m(t) = 1 \text{ au}(149 \text{ au})(t/T)^2$ for models (ii) and (iv), and $m(t) = 1 \text{ au}(199 \text{ au})(t/T)^2$ for model (iii). The propagation time was $T = 100\tau$, with $\tau = 0.1 \text{ au}$. The initial positions $x_k = 0.0 \text{ au}$ and $x_k = 3.5 \text{ au}$ were used for (i) and (ii)–(iv), respectively. All possible frequencies on the reciprocal time grid were used. For the dipole, an initial coefficient guess $\gamma_{xj} = 1.0$ and dipole constants with all possible combinations of $k_j = ((2\pi j)/(x_{\max} - x_{\min}))$, $l_n = (\pi n)/(\Delta x)$ were used, with $j = 0, \dots, 5$, $l = 0, \dots, (N_\gamma)/(100) - 1$ in a dipole of the form of eq 14.

In summary, Figure 7 shows that the QuOCO methodology can successfully locate global minima in rather challenging potentials with difficult obstacles. The optimizations for benchmark potentials (ii)–(iv) illustrate the capabilities of QuOCO as applied to minimization problems more challenging than model (i), including the search for more distant global minima (ii), narrower minima (iii), and the differentiation between global and local minima of similar depths (iv). While these model problems are typically difficult for a variety of alternative methods, we find that QuOCO is capable of solving such problems effectively due to the flexibility offered by an

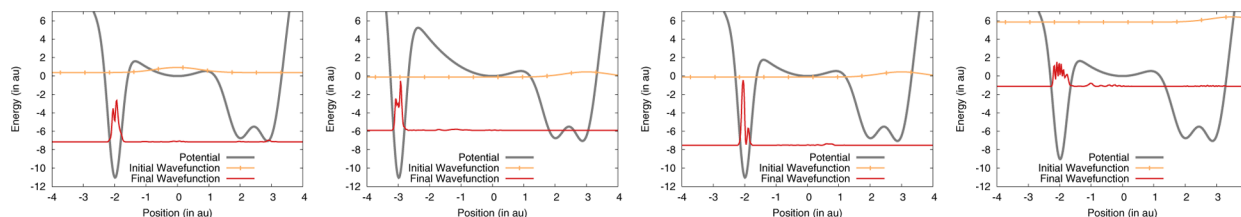


Figure 7. Golf potentials (i)–(iv) (gray line), parametrized according to Table 4, and final states (red line) after propagation of the initial state (orange line) with optimized controls found by QuOCO.

Table 4. Parameters (in au) of Golf Potentials Shown in Figure 7, Defined According to Eq 24, Including $x_{0,i}$, D_i , and S_i , with $i = 1-3$

| case | $x_{0,1}$ | D_1 | S_1 | $x_{0,2}$ | D_2 | S_2 | $x_{0,3}$ | D_3 | S_3 |
|-------|-----------|-------|-------|-----------|-------|-------|-----------|-------|-------|
| (i) | -2.0 | 15 | 10 | 2.0 | 10 | 3.0 | 3.0 | 15 | 3.0 |
| (ii) | -3.0 | 20 | 10 | 2.0 | 10 | 3.0 | 3.0 | 15 | 3.0 |
| (iii) | -2.0 | 15 | 12 | 2.0 | 10 | 3.0 | 3.0 | 15 | 3.0 |
| (iv) | -2.0 | 13 | 10 | 2.0 | 10 | 3.0 | 3.0 | 15 | 3.0 |

Table 5. Expectation Values (in au) of the Potential $\langle \hat{V}(T) \rangle$ and Position $\langle \hat{x}(T) \rangle$ as Follows, Standard Deviation (SD), and Number of Propagation Runs for Golf Potentials (i)–(iv)

| case | $\langle \hat{V}(T) \rangle$ | $\langle \hat{x}(T) \rangle$ | SD | # runs |
|-------|------------------------------|------------------------------|------|--------|
| (i) | -9.2 | -1.7 | 1.1 | 520 |
| (ii) | -8.9 | -2.8 | 0.40 | 395 |
| (iii) | -9.8 | -1.9 | 0.34 | 160 |
| (iv) | -5.7 | -1.6 | 1.2 | 450 |

extended set of controls that allow the system to gain energy from the field and surmount extended barriers separating local and global minima.

4. CONCLUSIONS

We have introduced the QuOCO methodology to perform steered quantum dynamics for energy minimization. The method combines the D-MORPH gradient and nonlinear optimization (most efficiently L-BFGS-B) based on an extended set of controls that define the time-dependent mass, dipole moment, and perturbational field. We have illustrated the resulting algorithm as applied to the search for global minima in potential energy surfaces with multiple wells, including the prototypical golf problem previously explored for testing quantum annealing methodologies, as well as more challenging minimization problems on rugged surfaces. When compared to naïve computation of gradients in N -dimensional control space via finite differencing (requires $N + 1$ propagations), the D-MORPH gradient is highly accurately evaluated in only four wavepacket propagations, independent of the number of controls, allowing for the addition of controls at little cost dominated by optimization in a larger space. The QuOCO method prescribes addition of control variables in a systematic fashion via series expansion of the controlled quantities so that the number of controls can always be converged to the point where the global minimum is found successfully. As currently formulated, the method requires wavepacket propagation, which is computationally demanding, although a variety of performant methods for wave packet propagation are available.^{76,77,84–101} Work in progress involves the implementation of QuOCO within the framework of

semiclassical dynamics for global minimization in high-dimensional potential energy surfaces.

5. APPENDIX 1

The gradients of the potential energy with respect to the control parameters,

$$\frac{\partial \langle \hat{V}_0(T; \beta) \rangle}{\partial \beta_j} = \left\langle \psi_i \left| \frac{\partial}{\partial \beta_j} [U^\dagger(T, 0, \beta) V_0(x) U(T, 0, \beta)] \right| \psi_i \right\rangle \quad (26)$$

can be computed according to eq 7 since

$$\begin{aligned} \frac{\partial}{\partial \beta_j} [U^\dagger(T, 0, \beta) V_0(x) U(T, 0, \beta)] \\ = (-i/\hbar) \int_0^T [U^\dagger(T, 0, \beta) V_0(x) U(T, t, \beta) \hat{H}_{\beta_j}(t', \beta) U(T, 0, \beta) \\ - U^\dagger(T, 0, \beta) \hat{H}_{\beta_j}(t', \beta) U^\dagger(t, T, \beta) V_0(x) U(T, 0, \beta)] dt \end{aligned} \quad (27)$$

where subscript β_j denotes the partial derivative with respect to β_j .

To derive eq 27, we consider that

$$\begin{aligned} \frac{\partial}{\partial \beta_j} [U^\dagger(T, 0, \beta) V_0(x) U(T, 0, \beta)] \\ = U_{\beta_j}^\dagger(T, 0, \beta) V_0(x) U(T, 0, \beta) + U^\dagger(T, 0, \beta) V_0(x) U_{\beta_j}(T, 0, \beta) \end{aligned} \quad (28)$$

where the propagator, introduced by eq 3, satisfies the time-dependent Schrödinger equation,

$$i\hbar \frac{\partial}{\partial t} U(t, 0, \beta) = \hat{H}(t, \beta) U(t, 0, \beta) \quad (29)$$

and its conjugate satisfies

$$-i\hbar \frac{\partial U^\dagger(t, 0, \beta)}{\partial t} = U^\dagger(t, 0, \beta) \hat{H}(t, \beta) \quad (30)$$

Its partial derivative with respect to β_j , U_{β_j} , satisfies the following equation:

$$i\hbar \frac{\partial}{\partial t} U_{\beta_j}(t, 0, \beta) = \hat{H}_{\beta_j}(t, \beta) U(t, 0, \beta) + \hat{H}(t, \beta) U_{\beta_j}(t, 0, \beta) \quad (31)$$

Therefore, according to eqs 31 and 30, we obtain

$$\begin{aligned} i\hbar \frac{\partial}{\partial t} [U^\dagger(t, 0) U_{\beta_j}(t, 0)] &= i\hbar \left[\frac{\partial U^\dagger(t, 0)}{\partial t} U_{\beta_j}(t, 0) + U^\dagger(t, 0) \frac{\partial U_{\beta_j}(t, 0)}{\partial t} \right] \\ &= -U^\dagger(t, 0) \hat{H}(t) U_{\beta_j}(t, 0) + U^\dagger(t, 0) \\ &\quad [H_{\beta_j}(\beta, t) U(t, 0) + \hat{H}(\beta, t) U_{\beta_j}(t, 0)] \\ &= U^\dagger(t, 0) H_{\beta_j}(\beta, t) U(t, 0). \end{aligned} \quad (32)$$

Integration with respect to time and multiplication by the forward propagator yields

$$\begin{aligned}
 U_{\beta_j}(t, 0) &= (-i/\hbar)U(t, 0) \int_0^t dt' U^\dagger(t', 0) H_{\beta_j}(\beta, t') U(t', 0) \\
 &= (-i/\hbar) \int_0^t dt' U(t, t') H_{\beta_j}(\beta, t') U(t', 0)
 \end{aligned}
 \quad (33)$$

and the conjugate of eq 33 gives

$$U_{\beta_j}^\dagger(t, 0) = (i/\hbar) \int_0^t dt' U^\dagger(t', 0) H_{\beta_j}(\beta, t') U^\dagger(t, t') \quad (34)$$

Substituting eqs 33 and 34 into eq 28 gives eq 27.

AUTHOR INFORMATION

Notes

The authors declare no competing financial interest.

ACKNOWLEDGMENTS

The authors are grateful to Bill Jorgensen for being a wonderful colleague. V.S.B. acknowledges support from the National Science Foundation Grant CHE 911520 and supercomputer time from NERSC and the Yale University Faculty of Arts and Sciences High Performance Computing Center partially funded by the National Science Foundation Grant CNS 08-21132. M.S. acknowledges financial support from the Arnold and Mabel Beckman Foundation. We also thank Professor H. Rabitz, A. Donovan, and D. Hocker for discussions on the D-MORPH method, Professor E. Denardo for stimulating discussions of current optimization algorithms, Professor J. E. Straub for pointing us to previous work, including refs 11, 26, 104, and 105, and Dr. V. Beltrani for ref 106.

REFERENCES

- (1) Lee, E. T. Optimization by a Gradient Technique. *Ind. Eng. Chem. Res.* **1964**, *3*, 373–380.
- (2) Stilling, F. H.; Rahman, A. Molecular Dynamics Study of Temperature Effects on Water Structure and Kinetics. *J. Chem. Phys.* **1972**, *57*, 1281–1292.
- (3) Witt, A.; Sebastianelli, F.; Tuckerman, M. E.; Bacic, Z. Path Integral Molecular Dynamics Study of Small H₂ Clusters in the Large Cage of Structure II Clathrate Hydrate: Temperature Dependence of Quantum Spatial Distributions. *J. Phys. Chem. C* **2010**, *114*, 20775–20782.
- (4) Yu, T. Q.; Tuckerman, M. E. Temperature-Accelerated Method for Exploring Polymorphism in Molecular Crystals Based on Free Energy. *Phys. Rev. Lett.* **2011**, *107*, 015701.
- (5) Hooke, R.; Jeeves, T. A. "Direct Search" Solution of Numerical and Statistical Problems. *JACM* **1961**, *8*, 212–229.
- (6) Spendley, W.; Hext, G. R.; Himsforth, F. R. Sequential Application of Simplex Designs in Optimisation and Evolutionary Operation. *Technometrics* **1962**, *4*, 441–461.
- (7) Nelder, J. A.; Mead, R. A Simplex Method for Function Minimization. *Comput. J.* **1965**, *7*, 308–313.
- (8) Levitt, M.; Lifson, S. Refinement of Protein Conformations Using a Macromolecular Energy Minimization Procedure. *J. Mol. Biol.* **1969**, *46*, 269–279.
- (9) Minary, P.; Tuckerman, M. E.; Martyna, G. J. Dynamical Spatial Warping: A Novel Method for the Conformational Sampling of Biophysical Structure. *SIAM* **2008**, *30*, 2055–2083.
- (10) Summa, C. M.; Levitt, M. Near-Native Structure Refinement Using in Vacuo Energy Minimization. *Proc. Natl. Acad. Sci. U.S.A.* **2007**, *104*, 3177–3182.
- (11) Andricioaei, I.; Straub, J. E. Finding the Needle in the Haystack: Algorithms for Conformational Optimization. *Comput. Phys.* **1996**, *10*, 449–454.
- (12) Land, A. H.; Doig, A. G. An Automatic Method of Solving Discrete Programming Problems. *Econometrica* **1960**, *28*, 497–520.
- (13) Little, J. D. C.; Murty, K. G.; Sweeney, D. W.; Karel, C. An Algorithm for the Traveling Salesman Problem. *Oper. Res.* **1963**, *11*, 972–989.
- (14) Becker, R. W.; Lago, G. V. *8th Allerton Conference on Circuits and Systems Theory* **1970**, 3–12.
- (15) Törn, A. A. *Computer Simulation Versus Analytical Solutions for Business and Economic Models*; University of Gothenburg: Gothenburg, Sweden, 1972; pp 191–206.
- (16) Glover, F.; McMillan, C.; Novick, B. Interactive Design Software and Computer Graphics for Architectural and Space Planning. *Ann. Oper. Res.* **1985**, *5*, 557–573.
- (17) Glover, F. Tabu Search Methods in Artificial Intelligence and Operations Research. *ORSA Artificial Intelligence* **1987**, *1*, 6.
- (18) Cavazos, J.; Moss, J. E. B.; O'Boyle, M. F. P. 15th International Conference on Compiler Construction, March 30–31, 2006, Vienna, Austria, ETAPS: Wien, Austria, 2006; pp 124138.
- (19) Cavicchio, D. J. *Adaptive Search Using Simulated Evolution*. Ph.D. thesis, Dept. Computer and Communication Sciences, Univ. of Michigan, Ann Arbor, MI, 1970.
- (20) Holland, J. H. *Adaptation in Natural and Artificial Systems: An Introductory Analysis with Applications to Biology, Control, and Artificial Intelligence*; University of Michigan Press: Ann Arbor, MI, 1975.
- (21) Fogel, L. J. Autonomous Automata. *Industrial Research Magazine* **1962**, *4*, 14–19.
- (22) Koza, J. R. Proceedings of the 11th International Joint Conference on Artificial Intelligence, Detroit, MI, August 20–25, 1989, Morgan Kaufmann Publishers: St. Simons Island, GA, 1989.
- (23) Koza, J. R. *Genetic Programming: A Paradigm for Genetically Breeding Populations of Computer Programs to Solve Problems*; Stanford University: Stanford, CA, 1990.
- (24) Dorigo, M.; Maniezzo, V.; Colnari, A. Ant System: Optimization by a Colony of Cooperating Agents. *IEEE Trans. Syst. Man. Cybern. B* **1996**, *26*, 29–41.
- (25) Kennedy, J.; Eberhart, R. Particle Swarm Optimization. *ICNN Proc.* **1995**, 1–6, 1942–1948.
- (26) Amara, P.; Hsu, D.; Straub, J. E. Global Energy Minimum Searches Using an Approximate Solution of the Imaginary Time Schroedinger Equation. *J. Phys. Chem.* **1993**, *97*, 6715–6721.
- (27) Finnila, A. B. Quantum Annealing: A New Method for Minimizing Multidimensional Functions. *Chem. Phys. Lett.* **1994**, *219*, 343–348.
- (28) Farhi, E.; Goldstone, J.; Gutmann, S.; Sipser, M. *arXiv:quant-ph/0001106*.
- (29) Liu, P.; Berne, B. J. Quantum Path Minimization: An Efficient Method for Global Optimization. *J. Chem. Phys.* **2003**, *118*, 2999–3005.
- (30) Kadowaki, T.; Nishimori, H. Quantum Annealing in the Transverse Ising Model. *Phys. Rev. E: Stat., Nonlinear, Soft Matter Phys.* **1998**, *58*, 5355–5363.
- (31) Shalloway, D. Application of the Renormalization Group to Deterministic Global Minimization of Molecular Conformation Energy Functions. *J. Global Optimization* **1992**, *2*, 281–311.
- (32) Ma, J.; Straub, J. E. Simulated Annealing Using the Classical Density Distribution. *J. Chem. Phys.* **1994**, *101*, 533–541.
- (33) Piela, L.; Kostrowicki, J.; Scheraga, H. A. On the Multiple-Minima Problem in the Conformational Analysis of Molecules: Deformation of the Potential Energy Hypersurface by the Diffusion Equation Method. *J. Phys. Chem.* **1989**, *93*, 3339–3346.
- (34) Kostrowicki, J.; Piela, L.; Cherayil, B. J.; Scheraga, H. A. Performance of the Diffusion Equation Method in Searches for Optimum Structures of Clusters of Lennard-Jones Atoms. *J. Phys. Chem.* **1991**, *95*, 4113–4119.
- (35) Stillinger, F. H.; Weber, T. A. Nonlinear Optimization Simplified by Hypersurface Deformation. *J. Stat. Phys.* **1988**, *52*, 1429–1445.
- (36) Pillardy, J.; Olszewski, K. A.; Piela, L. Performance of the Shift Method of Global Minimization in Searches for Optimum Structures of Clusters of Lennard-Jones Atoms. *J. Phys. Chem.* **1992**, *96*, 4337–4341.

- (37) Marcus, R. J.; Zvolinski, B. J.; Eyring, H. The Electron Tunneling Hypothesis for Electron Exchange Reactions. *J. Phys. Chem.* **1954**, *58*, 432–437.
- (38) Getteschi, D.; Sessoli, R. Quantum Tunneling of Magnetization and Related Phenomena in Molecular Materials. *Angew. Chem., Int. Ed.* **2003**, *42*, 268–297.
- (39) Santoro, G. E.; Martonák, R.; Tosatti, E.; Car, R. Theory of Quantum Annealing of an Ising Spin Glass. *Science* **2002**, *295*, 2427–2430.
- (40) Martonák, R.; Santoro, G. E.; Tosatti, E. Quantum Annealing of the Traveling-Salesman Problem. *Phys. Rev. E: Stat., Nonlinear, Soft Matter Phys.* **2004**, *70*, 057701.
- (41) Titiloye, O.; Crispin, A. Quantum Annealing of the Graph Coloring Problem. *Discrete Optimization* **2011**, *8*, 376–384.
- (42) Lee, Y. H.; Berne, B. J. Global Optimization: Quantum Thermal Annealing with Path Integral Monte Carlo. *J. Phys. Chem. A* **2000**, *104*, 86–95.
- (43) Lee, Y. H.; Berne, B. J. Quantum Thermal Annealing with Renormalization: Application to a Frustrated Model Protein. *J. Phys. Chem. A* **2001**, *105*, 459–464.
- (44) Battaglia, D. A.; Santoro, G. E.; Tosatti, E. Optimization by Quantum Annealing: Lessons from Hard Satisfiability Problems. *Phys. Rev. E: Stat., Nonlinear, Soft Matter Phys.* **2005**, *71*, 066707(10).
- (45) Sejnowski, T. J.; Hinton, G. E. In *Vision, Brain, and Computer*; Arbib, M. A., Hanson, A. R., Eds.; MIT Press: Cambridge, MA, 1986.
- (46) Baum, E. B. Intractable Computations without Local Minima. *Phys. Rev. Lett.* **1986**, *57*, 2764–2767.
- (47) Bernasconi, J. Low Autocorrelation Binary Sequences: Statistical Mechanics and Configuration Space Analysis. *J. Phys. (Paris)* **1987**, *48*, 559–567.
- (48) Dill, K. A. Polymer Principles and Protein Folding. *Protein Sci.* **1999**, *8*, 1166–1180.
- (49) Tovchigrechko, A.; Vakser, I. A. How Common Is the Funnel-Like Energy Landscape in Protein–Protein Interactions. *Protein Sci.* **2001**, *10*, 1572–1583.
- (50) Zhou, H.-X. Disparate Ionic-Strength Dependencies of On and Off Rates in Protein-Protein Association. *Biopolymers* **2001**, *59*, 427–433.
- (51) Locatelli, M. Simulated Annealing Algorithms for Continuous Global Optimization. In *Handbook of Global Optimization*; Pardalos, P. M., Romeijn, H. E., Eds.; Kluwer Academic Publishers: Dordrecht, The Netherlands, 2002; Vol. 2, pp 179–229.
- (52) Boltyanskii, V. G.; Gamkrelidze, R. V.; Pontryagin, L. S. On the Theory of Optimal Processes. *Dokl. Akad. Nauk SSSR* **1956**, *110*, 7–10.
- (53) Pontryagin, L. S.; Boltyanskii, V. G.; Gamkrelidze, R. V.; Mishechenko, E. F. In *The Mathematical Theory of Optimal Processes*; Bittner, L., Ed.; John Wiley and Sons: New York, 1962.
- (54) Rabitz, H. A.; Hsieh, M. M.; Rosenthal, C. M. Quantum Optimally Controlled Transition Landscapes. *Science* **2004**, *303*, 1998–2001.
- (55) Wu, R.; Rabitz, H.; Hsieh, M. Characterization of the Critical Submanifolds in Quantum Ensemble Control Landscapes. *J. Phys. A* **2008**, *41*, 015006.
- (56) Hsieh, M.; Wu, R.; Rabitz, H. Topology of the Quantum Control Landscape for Observables. *J. Chem. Phys.* **2009**, *130*, 104109.
- (57) Rothman, A.; Ho, T.-S.; Rabitz, H. Observable-Preserving Control of Quantum Dynamics over a Family of Related System. *Phys. Rev. A* **2005**, *72*, 023416.
- (58) Rothman, A.; Ho, T.-S.; Rabitz, H. A. Quantum Observable Homotopy Tracking Control. *J. Chem. Phys.* **2005**, *123*, 134104.
- (59) Ho, T.; Rabitz, H. Why Do Effective Quantum Controls Appear Easy to Find? *J. Photochem. Photobiol., A* **2006**, *180*, 226–240.
- (60) Beltrani, V.; Dominy, J.; Ho, T.-S.; Rabitz, H. Exploring the Top and Bottom of the Quantum Control Landscape. *J. Chem. Phys.* **2011**, *134*, 194106.
- (61) Runge, C. Ueber die numerische Auflösung von Differentialgleichungen. *Math. Ann.* **1895**, *46*, 167–178.
- (62) Kutta, W. Beitrag zur näherungsweise Integration von Differentialgleichungen. *Zeit. Math. Phys.* **1901**, *46*, 435–453.
- (63) Fletcher, R.; Powell, M. J. D. A Rapidly Convergent Descent Method for Minimization. *Comput. J.* **1963**, *6*, 163–168.
- (64) Broden, C. G. Quasi-Newton Methods and Their Application to Function Minimization. *Math. Comput.* **1967**, *21*, 368–381.
- (65) Broyden, C. G. The Convergence of a Class of Double-rank Minimization Algorithms 1. General Considerations. *J. Inst. Math. Appl.* **1970**, *6*, 76–90.
- (66) Goldfarb, D. A Family of Variable-Metric Methods Derived by Variational Means. *Math. Comput.* **1970**, *24*, 23–26.
- (67) Shanno, D. F. Conditioning of Quasi-Newton Methods for Function Minimization. *Math. Comput.* **1970**, *24*, 647–656.
- (68) Fletcher, R. *Practical Methods of Optimization*; John Wiley and Sons: Chichester and New York, 1987.
- (69) Irwin, A. W. FreeEOS. <http://freeeos.sourceforge.net/>.
- (70) Byrd, R. H.; Lu, P.; Nocedal, J. A Limited Memory Algorithm for Bound Constrained Optimization. *SIAM J. Sci. Stat. Comput.* **1995**, *16*, 1190–1208.
- (71) Zhu, C.; Byrd, R. H.; Nocedal, J. L-BFGS-B: Algorithm 778: L-BFGS-B, FORTRAN Routines for Large Scale Bound Constrained Optimization. *ACM Trans. Math. Software* **1997**, *23*, 550–560.
- (72) Morales, J. L.; Nocedal, J. L-BFGS-B: Remark on Algorithm 778: L-BFGS-B, FORTRAN Routines for Large Scale Bound Constrained Optimization. *ACM Trans. Math. Software* **2011**, *38*, 7:1–7:4.
- (73) Feit, M. D.; J. A. F., Jr.; Steiger, A. Solution of the Schrödinger Equation by a Spectral Method. *J. Comput. Phys.* **1982**, *47*, 412–433.
- (74) Feit, M. D.; Fleck, J. A., Jr. Solution of the Schrödinger Equation by a Spectral Method II: Vibrational Energy Levels of Triatomic Molecules. *J. Comput. Phys.* **1983**, *78*, 301–308.
- (75) Kosloff, D.; Kosloff, R. A Fourier Method Solution for the Time Dependent Schrödinger equation as a Tool in Molecular Dynamics. *J. Comput. Phys.* **1983**, *52*, 35–53.
- (76) Wu, Y.; Batista, V. S. Matching-Pursuit for Simulations of Quantum Processes. *J. Chem. Phys.* **2003**, *118*, 6720–6724.
- (77) Chen, X.; Batista, V. S. The MP/SOFT Methodology for Simulations of Quantum Dynamics: Model Study of the Photoisomerization of the Retinyl Chromophore in Visual Rhodopsin. *J. Photochem. Photobiol., A* **2007**, *190*, 274–282.
- (78) Kim, J.; Wu, Y.; Bredas, J.-L.; Batista, V. S. Quantum Dynamics of the Excited State Intramolecular Proton Transfer in 2-(2'-hydroxyphenyl)-benzothiazole. *Isr. J. Chem.* **2009**, *49*, 187–197.
- (79) Wu, Y.; Batista, V. S. Matching-Pursuit Split Operator Fourier Transform Simulations of Excited-State Intramolecular Proton Transfer in 2-(2'-hydroxyphenyl)-oxazole. *J. Chem. Phys.* **2006**, *124*, 224305.
- (80) Wu, Y.; Herman, M. F.; Batista, V. S. Matching-Pursuit Split Operator Fourier Transform Simulations of Nonadiabatic Quantum Dynamics. *J. Chem. Phys.* **2005**, *122*, 114114.
- (81) Chen, X.; Wu, Y.; Batista, V. S. Matching-Pursuit Split Operator Fourier Transform Computations of Thermal Correlation Functions. *J. Chem. Phys.* **2005**, *122*, 64102.
- (82) Wu, Y.; Batista, V. S. Quantum Tunneling in Multidimensional Systems: A Matching-Pursuit Description. *J. Chem. Phys.* **2004**, *121*, 1676–1680.
- (83) Wu, Y.; Batista, V. S. Erratum: Matching Pursuit for Simulations of Quantum Processes [J. Chem. Phys. 118, 6720, 2003]. *J. Chem. Phys.* **2003**, *119*, 7606.
- (84) Shalashilin, D. V.; Child, M. S. Time Dependent Quantum Propagation in Phase Space. *J. Chem. Phys.* **2000**, *113*, 10028–10036.
- (85) Shalashilin, D. V.; Child, M. S. Multidimensional Quantum Propagation with the Help of Coupled Coherent States. *J. Chem. Phys.* **2001**, *115*, 5367–5375.
- (86) Shalashilin, D. V. Quantum Mechanics with the Basis Set Guided by Ehrenfest Trajectories: Theory and Application to Spin-Boson Model. *J. Chem. Phys.* **2009**, *130*, 244101.
- (87) Shalashilin, D. V. Nonadiabatic Dynamics with the Help of Multiconfigurational Ehrenfest Method: Improved Theory and Fully

Quantum 24D Simulation of Pyrazine. *J. Chem. Phys.* **2010**, *132*, 244111.

(88) Saita, K.; Shalashilin, D. V. On-the-Fly Ab Initio Molecular Dynamics with Multiconfigurational Ehrenfest Method. *J. Chem. Phys.* **2012**, *137*, 22A506.

(89) Martínez, T. J.; Ben-Nun, M.; Levine, R. D. Multi-Electronic-State Molecular Dynamics: A Wave Function Approach with Applications. *J. Phys. Chem.* **1996**, *100*, 7884–7895.

(90) Martínez, T. J.; Levine, R. D. Non-Adiabatic Molecular Dynamics: Split-Operator Multiple Spawning with Applications to Photodissociation. *J. Chem. Soc., Faraday Trans.* **1997**, *93*, 941–947.

(91) Ben-Nun, M.; Martínez, T. J. A Multiple Spawning Approach to Tunneling Dynamics. *J. Chem. Phys.* **2000**, *112*, 6113–6121.

(92) Ben-Nun, M.; Martínez, T. J. Ab Initio Quantum Molecular Dynamics. In *Advances in Chemical Physics*; Prigogine, I., Rice, S. A., Eds.; John Wiley and Sons: New York, 2002; Vol. 121.

(93) Herman, M. F.; Kluk, E. A Semiclassical Justification for the Use of Non-Spreading Wavepackets in Dynamics Calculations. *Chem. Phys.* **1984**, *91*, 27–34.

(94) Kluk, E.; Herman, M. F.; Davis, H. L. Comparison of the Propagation of Semiclassical Frozen Gaussian Wave Functions with Quantum Propagation for a Highly Excited Anharmonic Oscillator. *J. Chem. Phys.* **1986**, *84*, 326–334.

(95) Billing, G. D. Quantum Corrections to the Classical Path Equations: Multitrajectory and Hermite Corrections. *J. Chem. Phys.* **1997**, *107*, 4286–4294.

(96) Billing, G. D. Mixed Quantum-Classical Methods. In *Encyclopedia of Computational Chemistry*; Schaefer, H. F., III, Ed.; Wiley: New York, 1998.

(97) Billing, G. D. Time-Dependent Quantum Dynamics in a Gauss-Hermite Basis. *J. Chem. Phys.* **1999**, *110*, 5526–5537.

(98) Burghardt, I.; Meyer, H. D.; Cederbaum, L. S. Approaches to the Approximate Treatment of Complex Molecular Systems by the Multiconfiguration Time-Dependent Hartree Method. *J. Chem. Phys.* **1999**, *111*, 2927–2939.

(99) Worth, G. A.; Robb, M. A.; Burghardt, I. *A Novel Algorithm for Non-Adiabatic Direct Dynamics Using Variational Gaussian Wavepackets*; Royal Society Chemistry: Cambridge, 2004; Vol. 127, pp 307–323.

(100) Lasorne, B.; Bearpark, M. J.; Robb, M. A.; Worth, G. A. Direct Quantum Dynamics Using Variational Multi-Configuration Gaussian Wavepackets. *Chem. Phys. Lett.* **2006**, *432*, 604–609.

(101) Lasorne, B.; Robb, M. A.; Worth, G. A. Direct Quantum Dynamics Using Variational Multi-Configuration Gaussian Wavepackets. Implementation Details and Test Case. *Phys. Chem. Chem. Phys.* **2007**, *9*, 3210–3227.

(102) Stillinger, F. H. Role of Potential-Energy Scaling in the Low-Temperature Relaxation Behavior of Amorphous Materials. *Phys. Rev. B* **1985**, *32*, 3134–3141.

(103) Shao, C. S.; Byrd, R. H.; Eskow, E.; Schnabel, R. B. In *Large-Scale Optimization with Applications, Part 3: Molecular Structure and Optimization*; Biegler, L. T., Coleman, T. F., Conn, A. R., Santosa, F. N., Eds.; IMA Vols in Mathematics and Its Applications; Univ. Minnesota Inst. Math. and Its Applicat.: Minneapolis, MN, 1995; Vol. 94, pp 163–199.

(104) Andricioaei, I.; Straub, J. E. Global Optimization Using Bad Derivatives: Derivative-Free Method for Molecular Energy Minimization. *J. Comput. Chem.* **19**, *13*, 1445–1455.

(105) Bicout, D. J.; Szabo, A. Entropic Barriers, Transition States, Funnels, and Exponential Protein Folding Kinetics: A Simple Model. *Protein Sci.* **2000**, *9*, 452–465.

(106) Beltrani, V.; Rabitz, H. Exploiting Time-Independent Hamiltonian Structure as Controls for Manipulating Quantum Dynamics. *J. Chem. Phys.* **2012**, *137*, 094109.